應用於平行非結構不可壓縮流解子的網格中心壓力基礎法

A Cell-Centered Pressure Based Method for Parallel Unstructured Incompressible Flow Solver[1]

陳驊[2]　黃培嘉[3]
Hua Chen[2] and George P.-G. Huang[3]

[2]立德管理學院資訊傳播學系
Leader University, Tainan, Taiwan
[3]肯塔基大學機械系
University of Kentucky, Lexington, KY, USA

摘　要

本文要介紹一可應用於非結構不可壓縮流場的網格中心壓力基礎法，本方法已實行在一新的二維/三維平行非結構網格計算流體力學程式來面對複雜幾何外型與邊界的物理問題，並同時能維持其高計算效率的特性。本方法在空間上使用二階上風法，在時間準確度上採用二階背向法。為了達到平行計算時的負載均衡，使用METIS來切割計算域。本文為了展示此法的準確性與計算效率，二維/三維空穴流、二維流體通過圓柱等問題被選擇來作為測試。在實際問題的應用上，汽車室內空調流場數值模擬的結果也在本文中展示，數值結果與實驗數據的比對也相當吻合。

關鍵詞：計算流體力學、壓力基礎法、不可壓縮、非結構格點、平行計算

Abstract

A cell-centered pressure based method for incompressible flow is presented in this paper, and it is implemented in a new two/three-dimensional parallel unstructured CFD code to meet the challenges of physical problems with complex geometries and complicated boundary conditions while maintaining high computational efficiency. The method uses a second order upwinding scheme in space and a second order backward scheme for time accuracy. The code is parallelized using METIS for domain decomposition with good load balancing across computational nodes. In order to demonstrate the accuracy and performance of current cell-centered pressure based method, two/three- dimensional driven cavity flow and two-dimensional flow over a circular cylinder are chosen for validation. In practical case, the simulated results of air-conditioned flow field in an automobile cabin are presented. All these test cases yielded good agreements in comparison with previous computational or experimental results.

Keyword：CFD, pressure based, incompressible, unstructured grid, parallel computing

---

[1] The support for this study under the 94S13 project of the Yen Tjing Ling Industrial Technology Research and Development Center is gratefully acknowledged.
[2] Assistant Professor, Dept. of Information Communication.
[3] Professor, Dept. of Mechanical Engineering, 151 Ralph G. Anderson Building.

1. Introduction

Over the past several decades, computational fluid dynamics (CFD) code has become a useful tool for fundamental research or industrial applications. As a result of continual improvements in computer technologies and CFD algorithms, numerical simulation with huge grid sizes and complex geometries are feasible. To deal with increasing grid sizes and demands for faster output, parallel computation of CFD has become a standard approach. Meanwhile, the challenges presented by some physical problems with complex geometries and complicated boundary conditions are now approached through unstructured CFD grids due to their ability to smoothly conform to complicated boundaries. However, combining unstructured grids with a parallel code presents still other challenges, such as achieving well-balanced grid decomposition on a distributed system and efficient parallel performance.

In order to meet these challenges, a cell-centered pressure based method has been implemented into a new parallel unstructured CFD code which is designed to meet the challenges of using unstructured grid codes. It is a two/three-dimensional finite volume incompressible Navier-Stokes solver. The code is second-order accurate in both time and space. To increase flexibility in complex geometries, a cell-centered pressure-based method is extended to use a variety of grid types, such as triangular, quadrilateral, tetrahedral, and hexahedral meshes. To obtain good load balancing across computational nodes, METIS [1] is applied for domain decomposition. METIS is a set of programs for partitioning graphs and finite element meshes, and for producing fill-reducing orderings for sparse matrices. The algorithms implemented in METIS are based on multilevel graph partitioning schemes. The parallel construction is based on message passing interface (MPI) protocols and has worked successfully on systems ranging from commodity PC clusters up to traditional supercomputers. In order to demonstrate the accuracy and performance of the cell-centered pressure-based method, several test cases are presented for validation.

2. Numerical Methods

A cell-centered pressure based method for two/three-dimensional finite volume unstructured incompressible Navier-Stokes solver for steady/unsteady flow fields is presented in this paper. The method described herein is based on SIMPLE algorithm with second order accuracy in both time and space. In order to compute numerical flux on interfaces, a second order upwind scheme is adopted to compute advection terms and second order central difference scheme is used for diffusion terms. A collocated grid system with the Rhie and Chow momentum interpolation method [2] is employed to avoid the checkerboard solution of the pressure based scheme.

2.1 Governing equations

The governing equations for unsteady incompressible viscous flow under the assumption of no body force and heat transfer are as below.

Conservation of Mass

$$\frac{\partial}{\partial t}\int_V \rho\, dV = -\oint_S \rho u_i n_i\, dS \tag{1}$$

Conservation of Momentum

$$\frac{\partial}{\partial t}\int_V \rho u_j dV = -\oint_S \rho u_i n_i\, u_j dS - \oint_S p n_j dS + \oint_S \tau_{ij}\, n_i dS \tag{2}$$

Conservation of Energy

$$\frac{\partial}{\partial t}\int_V \rho E dV = -\oint_S \rho u_i n_i\, E dS - \oint_S p u_j n_j dS + \oint_S u_j\, \tau_{ij} n_i dS \tag{3}$$

where ρ is density, p is pressure, u_i is component of velocity vector, n_i is unit normal vector of the interface, τ_{ij} is tensor of shear stress, and specific internal energy $E = e + \frac{1}{2}(u^2 + v^2 + w^2)$.

2.2 Center pressure based SIMPLE algorithm

By using an initial pressure field, P^n, we can obtain u^n, v^n, and w^n by solving the momentum equations in an sequential manner. The solution method is based on the 1st order delta form on the L.H.S and the momentum equations can be written in the form as Eq. (4).

$$\begin{aligned} a_c \Delta u &= \sum_{nb} a_{nb}\Delta u + RHS_u \\ a_c \Delta v &= \sum_{nb} a_{nb}\Delta v + RHS_v \\ a_c \Delta w &= \sum_{nb} a_{nb}\Delta w + RHS_w \end{aligned} \tag{4}$$

where the coefficients a_{nb} and a_c are

$a_{nb} = \max(-\dot{m}_f, 0) + \mu_f(\xi_x n_1 + \xi_y n_2 + \xi_z n_3)A$,

$a_c = \sum_{nb} a_{nb}$,

and the *RHS* term can be written as

$$RHS_u = -\sum_{i=1}^{N_{face}}[\dot{m}_i u_i^n - (\tau_{11}^n - p^n)_i n_{i,1} A_i - (\tau_{21}^n)_i n_{i,2} A_i - (\tau_{31}^n)_i n_{i,3} A_i]$$
$$= -\sum_{i=1}^{N_{face}}[\dot{m}_i u_i^n - (\tau_{11}^n)_i n_{i,1} A_i - (\tau_{21}^n)_i n_{i,2} A_i - (\tau_{31}^n)_i n_{i,3} A_i] - \frac{\partial p^n}{\partial x} V_c$$
$$RHS_v = -\sum_{i=1}^{N_{face}}[\dot{m}_i v_i^n - (\tau_{12}^n)_i n_{i,1} A_i - (\tau_{22}^n - p^n)_i n_{i,2} A_i - (\tau_{32}^n)_i n_{i,3} A_i]$$
$$= -\sum_{i=1}^{N_{face}}[\dot{m}_i v_i^n - (\tau_{12}^n)_i n_{i,1} A_i - (\tau_{22}^n)_i n_{i,2} A_i - (\tau_{32}^n)_i n_{i,3} A_i] - \frac{\partial p^n}{\partial y} V_c$$
$$RHS_w = -\sum_{i=1}^{N_{face}}[\dot{m}_i w_i^n - (\tau_{13}^n)_i n_{i,1} A_i - (\tau_{23}^n)_i n_{i,2} A_i - (\tau_{33}^n - p^n)_i n_{i,3} A_i]$$
$$= -\sum_{i=1}^{N_{face}}[\dot{m}_i w_i^n - (\tau_{13}^n)_i n_{i,1} A_i - (\tau_{23}^n)_i n_{i,2} A_i - (\tau_{33}^n)_i n_{i,3} A_i] - \frac{\partial p^n}{\partial w} V_c$$

where μ is dynamic viscosity, subscript *c* denotes the cell value to be solved, subscript *nb* denotes the neighbor cells, and *A* denotes the interfacial area. In this paper, Eq. (4) can be solved by using Gauss-Seidel point substitution. Then, we can obtain u*, v*, and w* by Eq. (5).

$$\begin{aligned} u^* &= u^n + \Delta u \\ v^* &= v^n + \Delta v \\ w^* &= w^n + \Delta w \end{aligned} \tag{5}$$

Although at this stage *u**, *v**, and *w** satisfy the momentum equations, they do not necessarily satisfy the continuity equation. In order to satisfy the mass conservation, one has to interpolate the velocity to the interface. In order to avoid the checkerboard solutions, one has to allow the interfacial velocity to be driven solely by the pressure difference evaluated directly at the interfaces. To achieve this aim without sacrificing the accuracy, one can divide the interpolated interfacial velocity into two components: one is the velocity component without the pressure contribution and the other is solely the pressure contribution. The former is first evaluated at the cell center as:

$$\begin{aligned} \tilde{u}^* &= u^* + \frac{\partial p^n}{\partial x}\frac{V_c}{a_c} \\ \tilde{v}^* &= v^* + \frac{\partial p^n}{\partial y}\frac{V_c}{a_c} \\ \tilde{w}^* &= w^* + \frac{\partial p^n}{\partial z}\frac{V_c}{a_c} \end{aligned} \tag{6}$$

and then interpolated into the cell faces. The latter is obtained directly from the pressure difference of the two adjacent nodal points, P_1 and P_2 such that the interfacial velocity can be expressed as:

$$\begin{aligned} u_f^* &= \tilde{u}_f^* - \left(\frac{\partial p^n}{\partial x}\right)_f \frac{V_f}{a_f} \\ v_f^* &= \tilde{v}_f^* - \left(\frac{\partial p^n}{\partial y}\right)_f \frac{V_f}{a_f} \\ w_f^* &= \tilde{w}_f^* - \left(\frac{\partial p^n}{\partial z}\right)_f \frac{V_f}{a_f} \end{aligned} \tag{7}$$

where V_f/a_f is obtained by interpolation from the cell center to the interface.

We further assume that there are corrections to u_f^*, v_f^*, and w_f^*, such that the continuity equation can be satisfied:

$$\sum_{i=1}^{N_{face}} \rho[(u_f^* + \Delta u_f')n_1 + (v_f^* + \Delta v_f')n_2 + (w_f^* + \Delta w_f')n_3]A = 0 \tag{8}$$

We can rewrite Eq. (8) as

$$\sum_{i=1}^{N_{face}} \rho[\Delta u_f' n_1 + \Delta v_f' n_2 + w_f' n_3]A = -\sum_{i=1}^{N_{face}} \rho[u_f^* n_1 + v_f^* n_2 + w_f^* n_3]A \tag{9}$$

where the right-hand side in Eq. (9) represents the mass imbalance in the control volume cell. One assumes there is a corresponding pressure correction field, *p′*, which drives the velocity corrections according to:

$$\begin{aligned} \Delta u_f' &\approx -\left(\frac{\partial p'}{\partial x}\right)_f \frac{V_f}{a_f} \approx -\frac{V_f}{a_f}\xi_x(p_{P_2}' - p_{P_1}') \\ \Delta v_f' &\approx -\left(\frac{\partial p'}{\partial y}\right)_f \frac{V_f}{a_f} \approx -\frac{V_f}{a_f}\xi_y(p_{P_2}' - p_{P_1}') \\ \Delta w_f' &\approx -\left(\frac{\partial p'}{\partial z}\right)_f \frac{V_f}{a_f} \approx -\frac{V_f}{a_f}\xi_z(p_{P_2}' - p_{P_1}') \end{aligned} \tag{10}$$

By substituting the velocity correction equations into the equation for the mass imbalance, we can obtain the equations of the pressure correction:

$$a_c p_c' = \sum_{nb} a_{nb} p_{nb}' + b \tag{11}$$

were a_{nb} and a_c in the continuity equation are

$$a_{nb} = \rho[\frac{V_f}{a_f}\xi_x n_1 + \frac{V_f}{a_f}\xi_y n_2 + \frac{V_f}{a_f}\xi_z n_3]A,$$

$$a_c = \sum_{nb} a_{nb},$$

and

$$b = -\sum_{nb} \rho[u_f^* n_1 + v_f^* n_2 + w_f^* n_3]A.$$

Once the pressure correction is obtained, one can update the pressure field by:

$$p^{n+1} = p^n + \alpha_p p' \tag{12}$$

where α_p is the under-relaxation factor for pressure and is generally with a value of 0.5-0.8. Then the velocity correction on the interfaces as well as

nodal points will be updated according to Eq. (7).

2.3 Partitioning approach

Figure 1 shows the schematic diagram of partitioning approach for cell-centered pressure based method. In Fig. 1, blue points (light points) indicate vertices, red points (dark points) indicate nodal points, and white points indicate the boundary points. By using this approach, the control volumes on the boundary are not split. Only communication of nodal values is needed for parallel computation which makes the implement of MPI in an unstructured grid more straightforward.

Excellent load balancing between the subgrids on each node is achieved through using METIS for domain decomposition. METIS can partition an unstructured grid into any integer number of zones without losing load balance. It is compatible with many platforms, convenient for running CFD codes on a variety of supercomputer to cluster architectures. Present partitioning approach has been tested by a number of two/three-dimensional geometries. All results show good load balances. The definition of load-imbalance rate L_{IMB} and load-balance rate L_B in this paper is defined as Eq. (13) and (14).

$$L_{IMB} = \frac{\left|N_{node} - N_{avg}\right|}{N_{avg}} \times 100\% \tag{13}$$

$$L_B = 1 - L_{IMB} \tag{14}$$

where N_{node} is grid size of the node and N_{avg} is the average grid size. By using load balance rate, we can compare the load balance quantitatively.

Figure 2(a) shows the partitioned grid for 2D flow over a circular cylinder in triangular mesh. The number of total grid points is 51,363 and the number of total cells is approximately 0.1M. The grid is partitioned to 16 zones for parallel computation. The cell distribution is not uniform, denser near the cylinder and coarser away. The load-balance distribution on each node is shown in Fig. 2(b). The x-axis indicates the node number and the y-axis indicates load-balance rate. The resulting load-balance rates are very close to 100% on every node with an average load balance rate of 98.37%. Various test cases have been made to prove the identical load balance. Our test results show that present partitioning approach has excellent load balance in two/three-dimensional grids with various types of meshes by using METIS for domain decomposition.

3. Results

3.1 Two-dimensional driven cavity flow

In this section, two-dimensional incompressible flow in a square cavity at a Reynolds number of 400 is simulated. The fluid in the cavity is driven by a moving top with constant speed. Because driven cavity flow lacks an exact solution, an existing accurate numerical solution for this problem is used as a benchmark for comparing our results. Ghia et al. [3] presented numerical studies using the vorticity-stream function formulation for solutions up to Re=10,000 with 257x257 grid points, and these simulation results have been widely used as a benchmark for the driven cavity problem. The schematic diagram of this case with geometry and boundary conditions is shown in Fig. 3. The initial condition for the entire computational domain is stationary everywhere. In order to compare Ghia's results, the number of grid points used is 257x257 or 66,049 and 65,536 cells are used in a quadrilateral mesh. For a triangular mesh, 66,546 cells, which is approximately the same as quadrilateral mesh, and 33,618 grid points are used in our computation. Figure 4(a) shows the u-velocity profile along the horizontal center line for both present results with quadrilateral and triangular mesh and Ghia's result. Both present results are in good agreement with Ghia's result. It also shows the present solution is identical and is independent of mesh types. Figure 4(b) shows the u-velocity profile along the horizontal center line; again, the results match. Figure 5 presents the streamline plot from the present results on the quadrilateral mesh. The flow structures including the location of the major vortex center, the bubble in the right bottom corner, and a small bubble in the left bottom corner are shown clearly in Fig. 5, and are in good agreement with the results of Ghia.

3.2 Three-dimensional driven cavity flow

The three-dimensional version of the preceding problem is also a standard case for a new flow solver. In 1987, Ku et al. [4] simulated three-dimensional flow in a cubic cavity by using pseudospectral methods to solve the Navier-Stokes equations for Re = 100, 400, and 1000. In 2003, Shu et al. [5] repeated this problem by using the SIMPLE algorithm with the differential quadrature (DQ) method. They simulated the three-dimensional driven cavity flow at Re = 100, 200, 400 and 1000 and compared their results with

Ku's results. In this section, we simulated this problem at Re = 400 and compared our results with those of Ku and Shu. In order to validate the results with different meshes, two grids are used to study this problem. One is a hexahedral mesh with 67x67x67 grid points and 287,496 cells, and the other is a tetrahedral mesh with 79,951 grid points and 446,953 cells. The geometry of this problem is a unit cube. The boundary condition at the y = 1 plane is uniform flow with u=1, v=0, and w=0, and all other boundary conditions are no-slip walls. The initial condition for the entire computational domain is stationary. Figure 6(a) shows the u-velocity profile at the horizontal centerline of the z = 0.5 plane for the present hexahedral and tetrahedral mesh results as well as those of Ku and Shu. Figure 6(b) shows the v-velocity profile at the vertical centerline of z = 0.5 for the same set of simulations. Both present simulations show essentially identical solutions and both are in good agreement with Ku and Shu.

3.3 Two-dimensional flow over a cylinder

Flow over a circular cylinder is a standard unsteady test problem. Figure 7 shows a schematic diagram for flow over a circular cylinder with dimensions and boundary conditions. The initial condition for the entire domain is uniform flow as inflow for all simulations and the time step is 0.005 for all cases. The grid for two-dimensional simulations is a quadrilateral mesh with 22705 cells and 22925 grid points and is densely distributed near the cylinder and wake region and coarser near the outer region. The Strouhal number (S_t) is derived from the frequency of coefficient of lift (C_L). The Strouhal number obtained from our results are 0.165 and 0.239 for Re=100 and 1000 respectively, which are in good agreement with other computational results. Fig. 8 shows the two-dimensional vorticity contours for Re = 100 and 1000. In Fig. 8, the contours are range from -0.3 to 0.3.

3.4 Air-conditioned flow field in an automobile cabin

As a result of the improvement of technology, the cabin equipments of automobiles are improved day by day. The thermal comfort in the automobile cabin has become important factor while consumers choosing new automobiles. Although computational fluid dynamics (CFD) has been developed to be a powerful design tool for industrial applications, there are only few papers about air-conditioned flow field in the automobile cabin. In order to quantify the thermal comfort, Fanger [6, 7, 8] empirically established the well known PMV (predicted mean vote) equation by using parameters relevant to thermal comfort. The thermal comfort that a human feels in indoor environment has been known to be influenced mostly by six parameters: air temperature, radiation, air flow, humidity, activity level and clothing thermal resistance. This section will focus on the air flow in the automobile cabin which is one of the six parameters of thermal comfort.

In this study, the experiment is made by using an available automobile Nissan SENTRA 2000. Figure 9 shows the cabin geometry with the air inlet and outlet, and the positions of experimental measuring points. The unit of length in Fig. 9 is meter, and the dimension is based on the real model. In this experiment, there are five points from x = 0.4 to 1.2m with 0.2m interval along the horizontal line and also five points from y = 0.4 to 0.8m with 0.1m interval along the vertical line at z = 0.71m plane as shown in Fig. 9. The measurement of velocity is implemented by using digital anemometer model DA30 with measuring range from 0.3 MPS to 35 MPS and accuracy ±2.5%. The summary of the experiments and numerical simulations is listed in Table 1. Figure 10 shows the partitioned grid for parallel computation. As shown in Fig. 10, tetrahedron mesh is used in our simulation and the computational domain is partitioned into 6 zones.

In this study, the characteristic length is the height of the inlet, 7 cm. The working fluid is air. The inlet velocities range between 2.7 and 7 m/s. According to these conditions, the Reynolds numbers of the simulations can be calculated. The range of Reynolds numbers are from 14,470 to 37,515. The turbulent model adopted in this study is F. R. Menter's SST model [11]. Figure 11 shows the comparison of numerical and experimental results. The label, 1st Exp., denotes the case of experiment with the 1st stage of wind speed. Similarly, other labels are referenced in Table 1. Figure 11(a) represents the comparisons of the velocity along the horizontal line. As shown in Fig. 11(a), current numerical results with laminar or turbulent models are in good agreement with the experimental results. Notably, the turbulent model gives a better result than the laminar result. Figure 11(b)

shows the comparison of velocity along the vertical line. As shown in Fig. 11(b), both results of laminar and turbulent models are unable to match the experimental data very well, especially the data on both ends. This is because the real air inlet has baffles which can help the flow to move further downstream and suppress diffusion of the flow, but current numerical simulation does not take this device into account. Therefore, the velocities measured from the experiment at y = 0.4m and 0.8m (two ends) approximate to zero as shown in Fig. 11(b), but the numerical results are not. Though numerical results show slight inaccuracy as the flow moving far away from the centerline of the inlet, the trends of the numerical results are similar to experimental data. In a word, the results show that current numerical method can successfully simulate this problem.

Comparing Figs. 12(a) with 12(b), turbulent flow seems to generate stronger circulation which causes the particles to move in spiral paths. As shown in Fig. 12(b), the circulations are observed both in the front seat and backseat, but this phenomenon does not appear in the laminar flow.

4. Conclusions

A cell-centered pressure based method is presented in this paper, and which has been applied to simulate incompressible flow fields successfully. Implementation of the cell-centered pressure based method into an unstructured CFD code is feasible and straightforward. In order to increase flexibility in complex geometries, cell-centered pressure based method has been extended to use a variety of grid types, such as triangular, quadrilateral, tetrahedral, and hexahedral meshes. By using METIS for domain decomposition, excellent parallel load balance is achieved. In this paper, the steady two and three-dimensional driven cavity flow, and unsteady two-dimensional flow over a circular cylinder are chosen for validation. In practical case, the air-conditioned flow field in the automobile cabin has been successfully simulated by presented method with laminar and turbulent models. All these test cases yielded good agreements in comparison with previous computational or experimental results.

References

[1] G. Karypis and V. Kumar, A software package for partitioning unstructured graphs, partitioning meshes, and computing fill-reducing orderings of sparse matrices version 4.0. http://www.cs.umn.edu/~karypis, 1998.

[2] C. M. Rhie and W. L. Chow, “Numerical study of the turbulent flow past an airfoil with tailing edge separation,” *AIAA J.*, Vol. 21, pp. 1525-1532, 1983.

[3] U. Ghia, K. N. Ghia, and C. T. Shin, “High-Resolution for Incompressible Flow Using the Navier-Stokes Equations and A Multigrid Method,” Journal of Computational Physics, Vol. 48, pp. 387-411, 1982.

[4] H. C. Ku, R. S. Hirsh, and T. D. Taylor, “A pseudospectral method for solution of the three-dimensional incompressible Navier-Stokes equations,” Journal of Computational Physics, Vol. 70, pp. 439-462, 1987.

[5] C. Shu, L. Wang, and Y. T. Chew, “Numerical Computation of Three-Dimensional Incompressible Navier-Stokes Equations in Primitive Variables Form by DQ method,” Int. J. Numer. Meth. Fluids, Vol. 43, pp. 345-368, 2003.

[6] P. O. Fanger, “Thermal Comfort – Analysis and Application in Environment Engineering,” Robert E. Krieger, Florida, 1982.

[7] P. O. Fanger et al., “Air Turbulence and Sensation of Draught,” Energy and Buidings, Vol. 12, pp. 21-39, 1988.

[8] P. O. Fanger, “A New Comfort Equation for Indoor Air Quality,” ASHRAE J., Vol. 31, pp. 33-38, 1989.

[9] H. Chen, P. G. Huang, and R. P. LeBeau, “Parallel 2D/3D Unsteady Incompressible Viscous Flow Computations Using an Unstructured CFD Code,” ICCFD3, Toronto, Canada, July 2004.

[10] H. Chen, P. G. Huang, and R. P. LeBeau, “A Center Pressure Based Method for Two/Three- dimensional Unstructured Navier-Stokes Solver,” AIAA paper 2005-0880, AIAA Aerospace Sciences Meeting and Exhibit, Reno, NV, Jan, 2005.

[11] F. R. Menter, “Two-Equation Eddy-Viscosity Turbulence Models For Engineering Applications,” *AIAA J.*, vol. 32, pp. 1598-1605, 1994.

Table 1 The summary of the experimental measurements and numerical simulations

Stage of wind speed		Exp.	Numerical simulation	
			Laminar	Turbulent
1	**2.7m/s**	√	√	√
2	**4.32m/s**	√	√	√
3	**6m/s**	√	√	√
4	**7m/s**	√	√	√

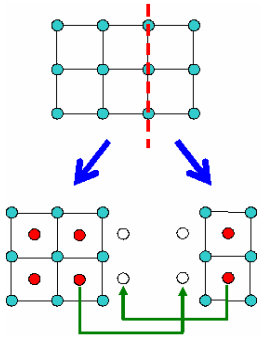

Fig. 1 A schematic diagram of cell-centered partitioning approach.

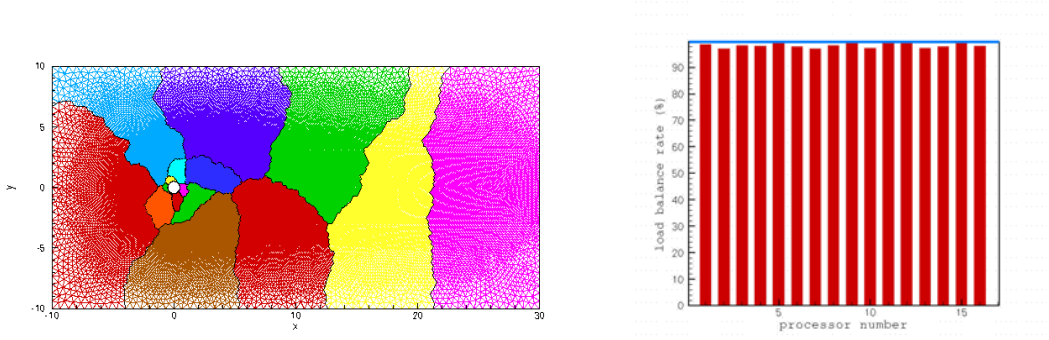

(a) (b)

Fig. 2(a) Partitioned triangular mesh for 2D flow over a circular cylinder; (b)Load-balance distribution on each node in parallel computation.

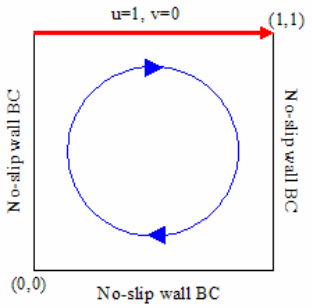

Fig. 3 The schematic diagram of two-dimensional driven cavity flow with boundary conditions.

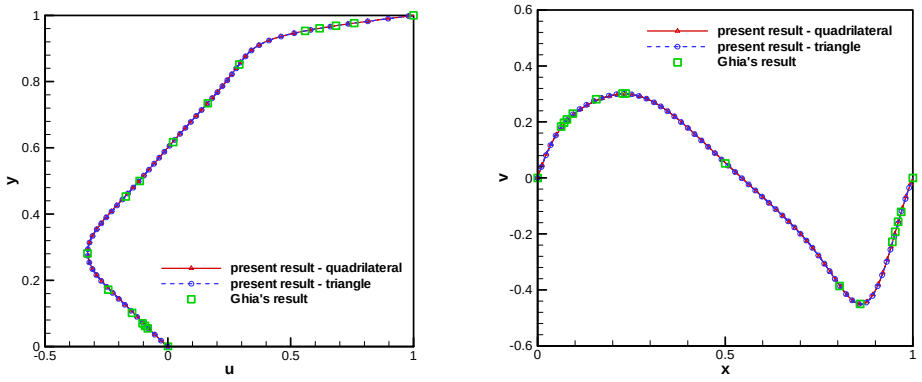

(a) (b)

Fig. 4(a) The u-velocity profile along the horizontal center line for present results and Ghia's result;(b)The v-velocity profile along the vertical center line for present results and Ghia's result.

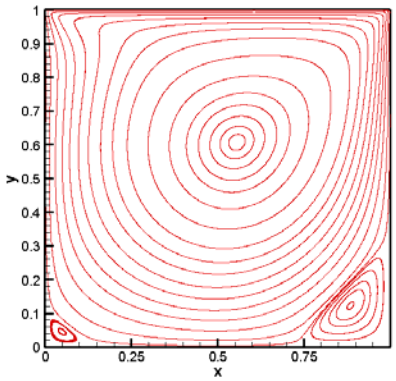

Fig. 5 Streamline plot for two-dimensional driven cavity flow at Re=400.

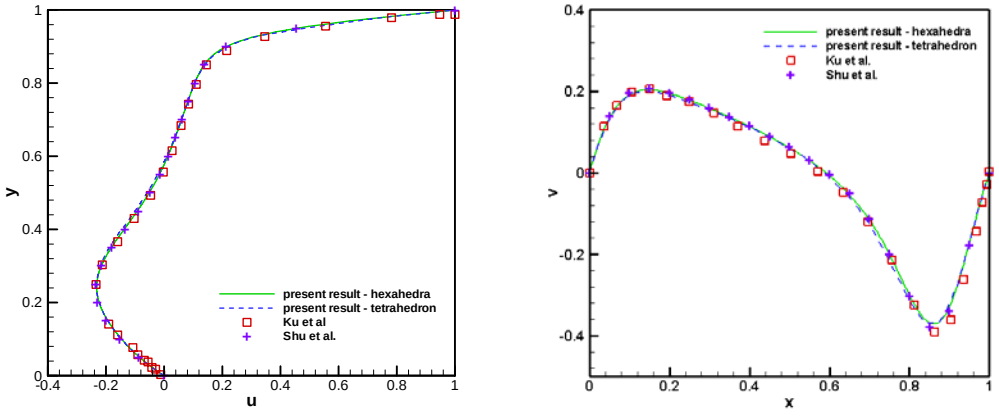

(a) (b)

Figure 6(a) The u-velocity profile at the horizontal centerline of z=0.5 plane;(b) The v-velocity profile at the vertical centerline of z=0.5 plane with present results, Ku's and Shu's results.

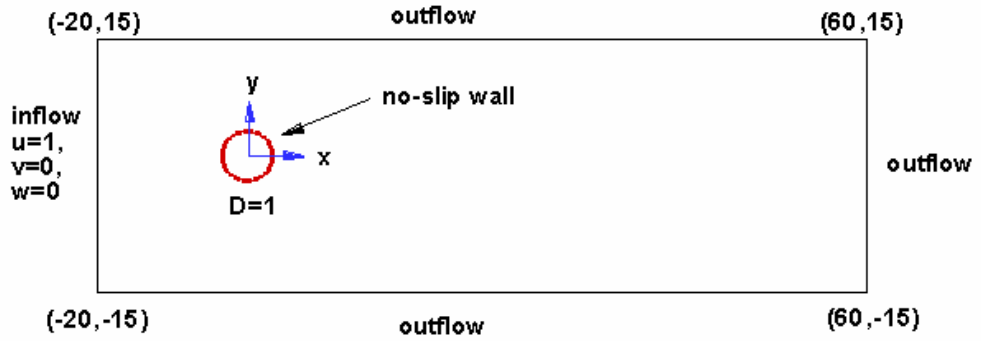

Fig. 7 Schematic diagram of flow over a circular cylinder with dimensions and boundary conditions.

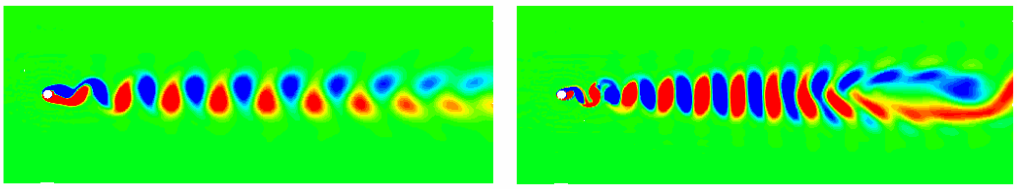

(a) (b)

Fig. 8 Vorticity contours for two-dimensional simulation. (a)Re=100 and (b)Re=1000.

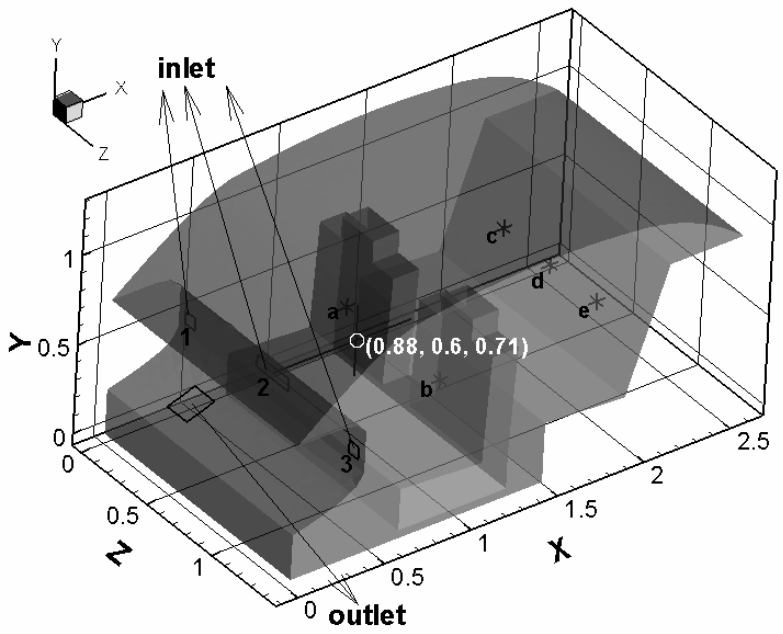

Fig. 9 A schematic diagram of cabin geometry with the air inlet and outlet, and the positions of experimental measuring points.

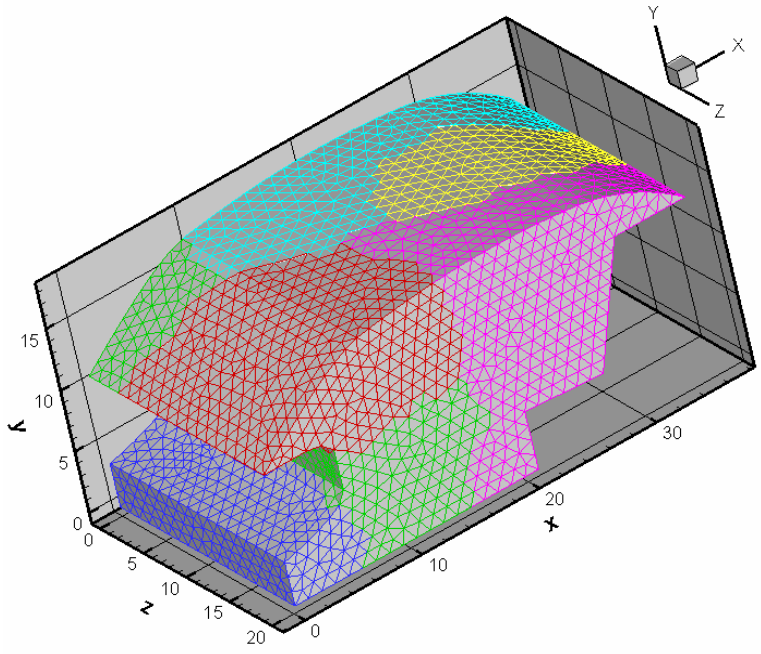

Fig. 10 The picture of partitioned computational domain.

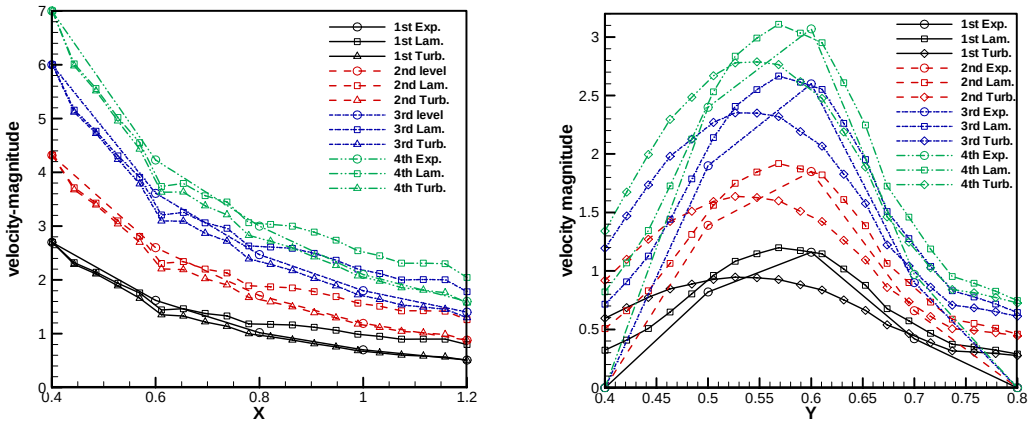

(a) (b)

Fig. 11(a) The comparison between numerical and experimental results for velocity along the horizontal line; (b) The comparison for velocity along the vertical line.

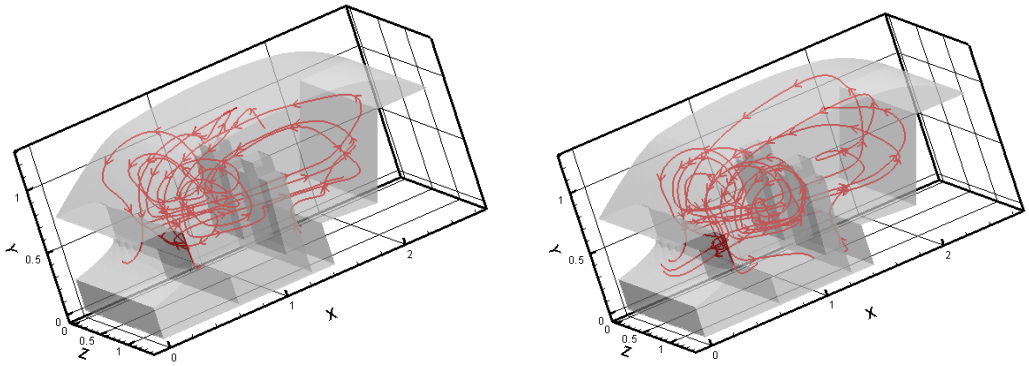

Fig. 12 The pictures of the particle paths of turbulent and laminar flow at 4st stage of wind speed, where (a) laminar flow and (b) turbulent flow.